Comparison of OVERFLOW Computational and Experimental Results for a Blunt Mars Entry Vehicle Concept during Supersonic Retropropulsion

Logan D. Halstrom*, Thomas H. Pulliam† , Robert E. Childs‡ , and Paul M. Stremel§, and Patrick J. Moran¶
NASA Ames Reseach Center, Moffett Field, CA, 94035

Simulations of unsteady supersonic retropropulsion (SRP) flow over a Hypersonic Inflatable Aerodynamic Decelerator (HIAD) blunt-body vehicle were performed using the OVERFLOW Computational Fluid Dynamics (CFD) solver. High-fidelity flow solver techniques, including Detached Eddy Simulation (DES) turbulence modeling and Adaptive Mesh Refinement (AMR), were employed to obtain improved realism in CFD predictions. Simulation conditions and geometry configurations were designed to match specific runs in the Descent System Study (DSS) wind tunnel testing (WTT) campaign. The accuracy of each simulation is assessed by direct comparison to experimental data. Comparisons of computational predictions of the SRP flowfield and bow shock shape to experimental schlieren imaging show reasonable prediction of mean shock shape, with approximately 10 % similarity in shock standoff distance for selected conditions, as well as similarity in local, time-varying fluctuations of the shock-plume interaction. Comparisons of discrete measurements of surface pressure coefficient (C_P) indicate CFD accuracy within approximately 10 % of the experiment across the majority of the model heatshield, with larger variations at some of the heatshield edge locations with stronger flow unsteadiness. Simulated unsteadiness of these chaotic flows, which were highly dynamic and multi-modal, was shown to be within 20-40 % of experimentally-measured pressure standard deviation (SD) for the majority of the sampled locations.

Nomenclature

Symbols

C_D	=	drag force coefficient
C_P	=	pressure coefficient
C_T	=	thrust coefficient
L/D	=	lift-to-drag ratio
M	=	Mach number
α	=	angle of attack

Acronyms

AETC	=	Aerosciences Evaluation and Test Capabilities
AMR	=	Adaptive Mesh Refinement
ARMD	=	Aeronautics Research Mission Directorate

*Aerospace Engineer, Systems Analysis Office (ARC-AA), AIAA Member, logan.halstrom@nasa.gov
†Senior Research Scientist, Science & Technology Corporation, AIAA Associate Fellow
‡Senior Research Scientist, Science & Technology Corporation
§Senior Research Scientist, Science & Technology Corporation, AIAA Member
¶Computer Scientist, Advanced Computing Branch (ARC-TNC)

BC	=	boundary condition
BDF2	=	Backwards Differentiation Formula
CAD	=	Computer Aided Design
CC	=	compressibility correction
CFD	=	Computational Fluid Dynamics
DES	=	Detached Eddy Simulation
DSS	=	Descent System Study
EDL	=	Entry, Descent, and Landing
GCD	=	Game Changing Development
HIAD	=	Hypersonic Inflatable Aerodynamic Decelerator
HLLC	=	Harten-Lax-van Leer-Contact
HLLE++	=	Harten-Lax-van Leer-Einfeldt
LES	=	Large Eddy Simulation
LUPWT	=	Langley Unitary Plan Wind Tunnel
NASA	=	National Aeronautics and Space Administration
PSP	=	Pressure-sensitive Paint
QCR	=	Quadratic Constitutive Relation
RANS	=	Reynolds-averaged Navier-Stokes
RC	=	rotation and curvature
RHS	=	Right Hand Side
RRM	=	Reverse Running Mean
SD	=	standard deviation
SRP	=	supersonic retropropulsion
SSOR	=	Symmetric Successive Over-Relaxation
SST	=	Shear Stress Transport
STMD	=	Space Technology Mission Directorate
URANS	=	Unsteady Reynolds-averaged Navier-Stokes
WTT	=	wind tunnel test

I. Introduction

Human exploration of Mars is an ongoing focus of science and technology development at the National Aeronautics and Space Administration (NASA) and other organizations. A key technical challenge is the ability to safely and reliably land large payloads on the planet's surface. The Martian atmosphere has a relatively low average density, which diminishes the effectiveness of aerodynamic drag deceleration techniques traditionally employed for Earth atmospheric reentry, but still requires shielding from aerothermodynamic heating and active control during powered descent. Recent NASA robotics missions have successfully employed a combination of a hypersonic aeroshell, a supersonic parachute, subsonic retropropulsion, and a sky crane manuever for Martian Entry, Descent, and Landing (EDL) [1]. However, NASA's critical mission requirement for future EDL vehicles is a payload capacity on the order of twenty metric tons, which is twenty times greater than current capabilities. These future missions, which include both precursor robotic and follow-on human landings, will forego the use of parachutes for supersonic deceleration due to the prohibitively large canopy sizes that would be required for these heavy-mass payloads. Instead, these missions are envisioned to employ supersonic retropropulsion (SRP) and powered descent for the latter stages of Martian EDL [2, 3]. One such vehicle concept is the low-L/D Hypersonic Inflatable Aerodynamic Decelerator (HIAD) [4], depicted in Fig. 1. This blunt body concept features a deployable aeroshell that enables traditional aerodynamic deceleration from orbital velocity down to $M \sim 2$, after which propulsive rocket engines integrated into the structure are used for final deceleration and landing.

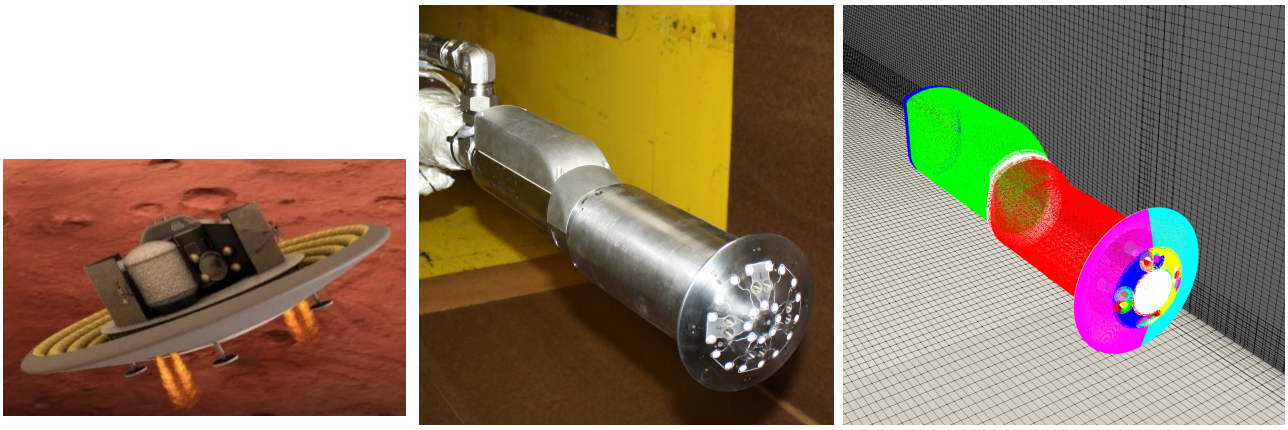

(a) Artist concept [2] **(b) Wind tunnel test model [5]** **(c) CFD mesh with truncated sting**

Fig. 1 Concept HIAD Mars EDL vehicle for human exploration missions

Development of these concept vehicles requires a thorough understanding of the complex aerodynamics associated with SRP, which can be challenging to obtain. A typical SRP flowfield is characterized by a bow shock supported by back-pressure from turbulent jets, which often results in unsteady fluctuations of the shock shape. Between the bow shock and vehicle surface is a complex environment of rocket plume shear layers interacting with mixed regions of strong normal shocks and weak oblique shocks that can dramatically alter the dynamic pressure in the post-shock region. Ground testing of these complex flows requires innovative model design and sophisticated data acquisition techniques. Additionally, the actual conditions of hot jets in the low-pressure, low-density, primarily-CO_2 Martian atmosphere are difficult to recreate in ground testing on Earth. Computational Fluid Dynamics (CFD) is a powerful tool that offers unique abilities to enhance and expand upon the SRP testing capabilities of traditional wind tunnel facilities. With its ability to model an extensive range of conditions, CFD can first be validated against terrestrially-acquired experimental data and then extended to Martian flight conditions. However, accurate simulation of the full complexity of SRP flow requires exceptional rigor in the development and application of CFD modeling best practices for spatial resolution and temporal convergence, and experimental validation is key for calibrating and establishing quantifiable computational accuracy.

With the objective of assessing the relative merits of wind tunnel test (WTT) and CFD methods for fulfilling future aerodynamic data-generation needs, an extensive campaign of SRP wind tunnel testing and analogous CFD simulation has been conducted under the NASA Aerosciences Evaluation and Test Capabilities (AETC) portfolio office. A primary criterion of this effort is the ability of CFD to provide vehicle aerodynamics data that is of "sufficient accuracy and reliability" to that produced by wind tunnel experiments. Ross et al. provide a detailed description of the objectives and scope of this effort [6]. This paper will discuss the study of SRP on the HIAD concept vehicle that was conducted as one component of this campaign done in partnership with the Descent System Study (DSS) under the Game Changing Development (GCD) program of NASA's Space Technology Mission Directorate (STMD).

A. Experiment Overview

The experimental data presented in this study was obtained in a wind tunnel test that was conducted in the spring of 2023 in the NASA Langley Unitary Plan Wind Tunnel (LUPWT). Extensive variations of conditions and models were tested, including six unique HIAD nozzle configurations as well as the mid-L/D CobraMRV configuration. Data was collected over the following range of Mach number (M), engine nozzle thrust coefficient (C_T), and angle of attack (α) conditions: $M = \{2.386, 3.477\}, C_T \in [0.5, 1.89], \alpha \in [-10°, 10°]$. Edquist et al. provide a detailed description of the scope and results of this experiment [5].

Experimental data was collected in a variety of forms including: static and dynamic surface pressure tap measurements, schlieren imaging, Pressure-sensitive Paint (PSP) imaging, and vehicle balance loads. Each test point was held on condition for a data collection interval of two seconds. Schlieren imaging of instantaneous variations in the flowfield refractive index was captured at a rate of 10 000 Hz and provides insight into both the unsteady and mean nature of the SRP flowfield and structure of the shock-plume interaction. Analogous computational schlieren images were

produced from CFD solutions for direct comparison to experiment using the ray tracing utility `raycast` [7]. Mean schlieren images were created for each condition by averaging 100 frames for each test point. Mean representations of the schlieren data were obtained for the experiment by averaging 100 instantaneous frames for each test point. Mean computational schlieren were produced by applying the `raycast` process to the time-averaged CFD flow solution. Average surface pressure measurements were collected by static pressure taps at discrete locations indicated in Fig. 2 by the black-circled numbers. Dynamic pressure measurements were collected at 20 000 Hz using kulite® sensors at locations indicated by red-squared numbers. Additional static and dynamic taps (not shown) were located on the vehicle backshell and support sting in the base pressure region. Test runs were also conducted to collect PSP imaging of the mean heatshield pressure distribution, however, damage occurred to the paint during reconfiguration of the model's removable engine nozzle inserts, which resulted in significant calibration error. Additionally, a novel, flow-through balance was equipped for the HIAD in order to measure vehicle loads and estimate nozzle thrust, but high sensitivity to flow temperature resulted in significant measurement uncertainty. CFD comparisons were not made to experimental results for PSP surface pressure and balance loads due to the significant uncertainty contained in these measurements.

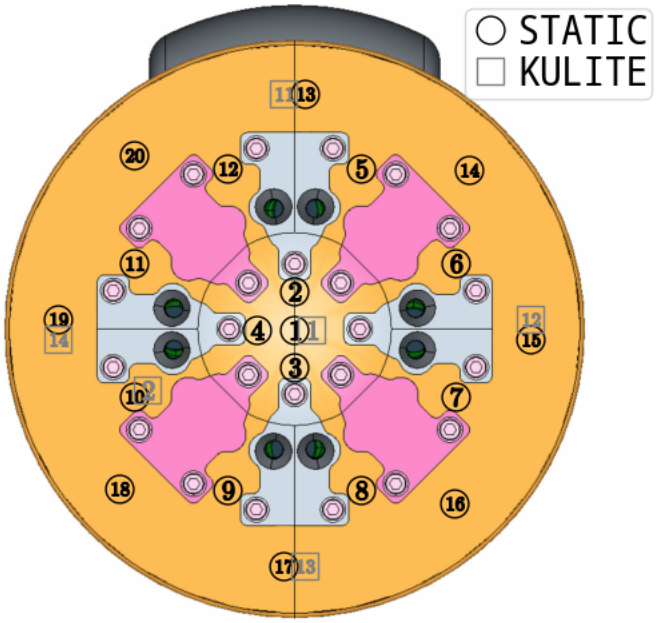

Fig. 2 HIAD model 1F engine nozzle and pressure instrument locations

B. Simulation Overview

This paper describes predictions of the aerodynamics of the HIAD concept using the OVERFLOW CFD solver and provides detailed comparisons of these results to experimental data for specific conditions. Section II of this paper summarizes the CFD solver procedure and computational domain utilized for the simulations presented in this work. Section III discusses the SRP flow behaviors observed in the OVERFLOW HIAD simulations and provides comparisons between computational and experimental results. This paper is published as part of a special AIAA session, which includes an overview of the experiment [5] and of the results simulated with OVERFLOW and several other CFD solvers [8] in conjunction with the wind tunnel test. The special session also contains an additional specific analysis using OVERFLOW by Matsuno et al. for the mid-L/D CobraMRV concept vehicle [9].

This paper will focus specifically on the the HIAD model 1F nozzle configuration, depicted in Fig. 2, which features paired engine nozzle clusters rather than a radially-symmetric distribution like all of the other models. This model demonstrated stronger and more chaotic flow unsteadiness in pre-test CFD simulations [10], so it was selected as the most challenging application for detailed post-test simulation and analysis. Specific comparisons between WTT and CFD results will be made in this analysis for the $M = 3.5, C_T = 1.89, \alpha = \{0°, -10°\}$ test points.

II. Computational Methodology

CFD simulations were performed using OVERFLOW, which is an implicit Navier-Stokes solver that employs finite-differencing methods on structured, overset grids [11–14]. Overset grid systems were developed using Chimera Grid Tools (CGT) [15–17] and its associated Graphic User Interface (GUI) Overgrid [16]. Overset region communication, interpolation stencils, and cell blanking were computed using Domain Connectivity Function (DCF) [18, 19].

A. Numerical Methods

1. CFD Process

All solutions were computed using a time-accurate solver with Newton sub-iterations at each time step to improve convergence. Time step size was determined by successively decreasing the step size until the general unsteady flow behavior remained consistent between changes. A non-dimensional time step of 0.01 was selected for these simulations, which equates to a freestream convection of 0.01 in (or 0.2 % of the heatshield diameter) per time step. Time was advanced implicitly using the 2nd-order Backwards Differentiation Formula (BDF2) with Symmetric Successive Over-Relaxation (SSOR) for the sub-iteration solver. The Harten-Lax-van Leer-Contact (HLLC) upwind spatial discretization scheme was employed with the van Albada limiter throughout the tunnel test section and near-body region, while the Harten-Lax-van Leer-Einfeldt (HLLE++) upwind scheme was applied locally in the bow shock region with the Koren limiter to promote more robust shock capturing.

Pre-test simulations completed with time-accurate Reynolds-averaged Navier-Stokes (RANS) or Unsteady Reynolds-averaged Navier-Stokes (URANS) demonstrated significant difference with experiment for vehicle drag at certain conditions due to turbulence modeling methodology, and it was determined that higher-fidelity Detached Eddy Simulation (DES) turbulence modeling was required to accurately resolve the fine length scales and the highly dynamic unsteadiness of the SRP shock-plume interaction [10]. All post-test DES simulations were initialized with time-accurate URANS, which was allowed to converge, at which point DES was initialized and allowed to iterate for a sufficient number of time steps to propagate URANS modeling transients downstream. The two-equation Shear Stress Transport (SST) RANS turbulence model [20] was employed in the hybrid-Large Eddy Simulation (LES) model, as it has been shown to be more accurate than other models available in OVERFLOW for flows with rocket plumes and other significant non-wall-bounded shear layers, such as the Orion Launch Abort Vehicle and reentry crew module, for which extensive experimental data was available for model validation [21, 22].

In addition to DES, specific turbulence modeling options were found to be critical for obtaining the best possible CFD accuracy for SRP applications. It was found that the combination of enabling the rotation and curvature (RC) option and disabling the compressibility correction (CC) option produced the most realistic predictions for SRP flow. Though this combination is not suitable for all types of high speed jets, it works well for the underexpanded ones modeled in this work. It was also found that the Quadratic Constitutive Relation (QCR) model [23, 24] improves the accuracy of tunnel wall corner flow vortex prediction. For post-test simulations, QCR was set to be active throughout the entire computational domain, as with DES, QCR is applied directly within the viscous fluxes and is only altered by DES through the reduced eddy-viscosity. This implementation differs from pre-test URANS cases, where QCR was limited to only the wall regions to avoid adverse effects in the plume shear layer solution. Additional, detailed discussion on the turbulence modeling of plume shear layers can be found in the companion paper by Childs and Matsuno[25].

2. Temporal Convergence

Simulations for this analysis were highly unsteady and required significant iteration to achieve temporal convergence over a statistically significant time interval. Simulation convergence was assessed both in terms of the solver and the time-averaging statistics. Convergence of the flow solver was determined by the Right Hand Side (RHS) matrix L2 residual norm, and the number of sub-iterations were chosen to achieve two orders of magnitude drop, at minimum.

Time-accurate convergence was assessed using an Reverse Running Mean (RRM) technique, where a window of convergence is determined starting from the latest iteration and moving backward in time until the mean computed over the window stabilizes, indicating that the average is statistically stationary over that interval. The running mean and standard deviation (SD) (depicted in Fig. 3 as a dashed black line and gray shaded region, respectively) are computed in a recursive fashion using Welford's online algorithm [26]. For the given example, the RRM "levels-out" or stabilizes at approximately 0.045 s of physical time, as indicated by the beginning of the selected averaging window depicted by the vertical red lines. It is also important that the beginning of the interval is selected such that no startup transients from previous run settings are contained in the average (e.g. non-zero-slope RRM immediate after the beginning of the `i5`

run sequence) and that the end of the interval must be in-family with the rest of the averaging interval and cannot exhibit sharp divergence in trend.

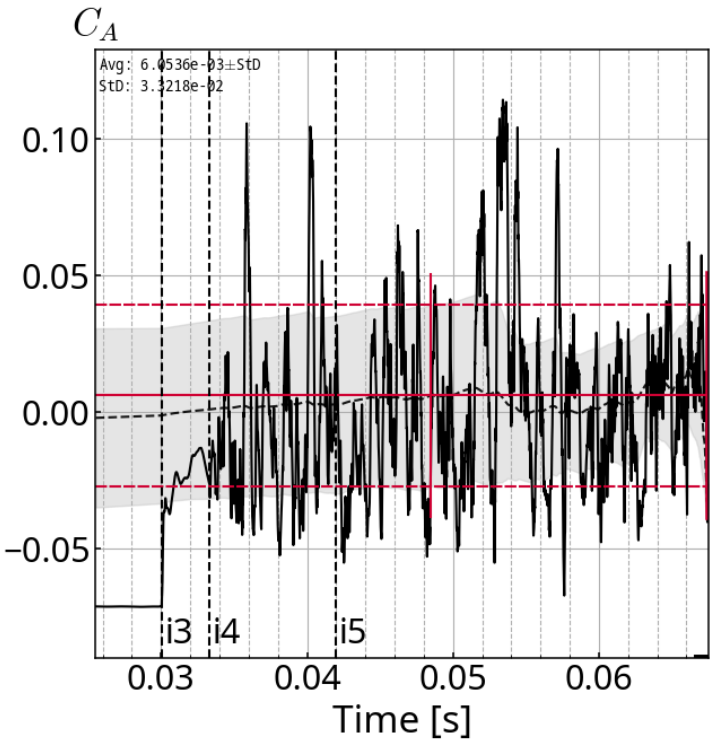

Fig. 3 The Reverse Running Mean temporal convergence assessment technique applied to OVERFLOW DES simulated integrated loads

B. Overset Grid System

The overset grid system for the CFD simulations conducted for this work consists of a segment of the LUPWT geometry containing the test section and the HIAD vehicle mounted to a truncated representation of the wind tunnel sting, as depicted in Fig. 4a. All CFD grids were designed from Computer Aided Design (CAD) models of the wind tunnel and test articles. The inflow boundary condition (BC) to the test section grid is derived from a simulation of the "full-empty-tunnel", as described below, and is prescribed at the constant-x plane indicated in Fig. 4a, which is twenty heatshield diameters forward of the vehicle model. Exit flow is modeled over an additional twenty-two diameters through the aft geometry of the wind tunnel test section, which contains two pressure-recovery compression ramps. The vehicle and sting near-body volume grids are encompassed in a surrounding coarse box grid shown in Fig. 4b, within which Adaptive Mesh Refinement (AMR) is activated to refine the mesh locally in regions where SRP flow features like the rocket plumes and bow shock are computed.

As visualized in the comparison of Figs. 4a and 4c, the computational representation of the model support sting was truncated at the backwards-facing step of the maximum-thickness portion of the housing for simplicity of modeling. Later modifications to accommodate the added flow-through balance resulted in a wind tunnel sting that was slightly elongated and of larger diameter than the original CAD design. As the freestream flow is supersonic, these downstream geometry differences do not have a significant influence on the upstream SRP flow interaction or the heatshield pressure distribution.

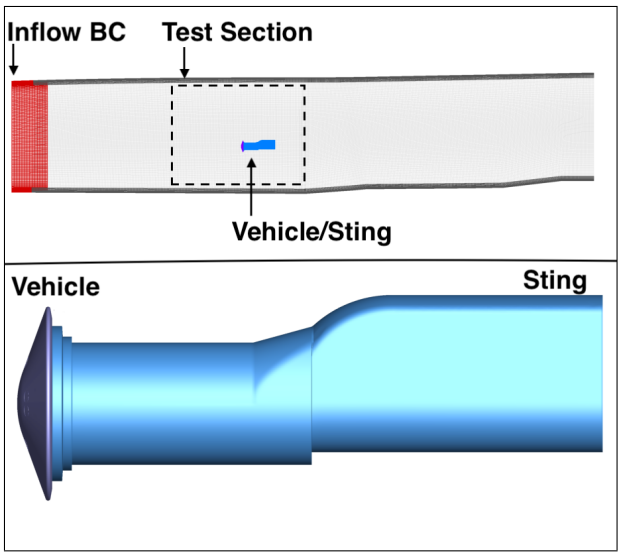

(a) Wind tunnel test section boundary conditions and vehicle surface geometry

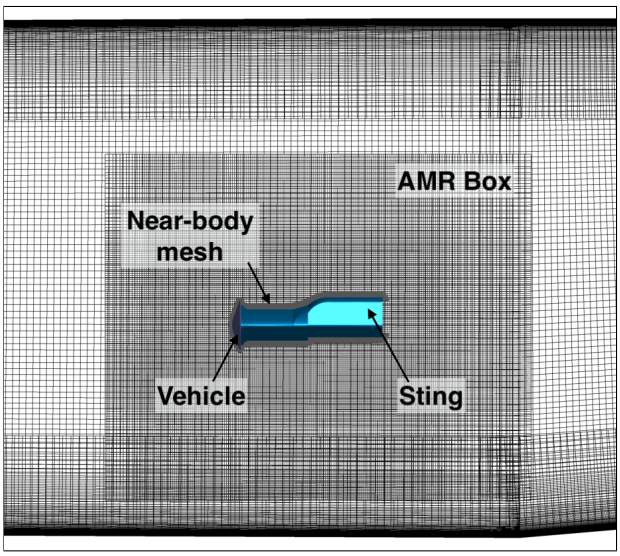

(b) Near-body volume grid and overlaid shock/plume refinement box

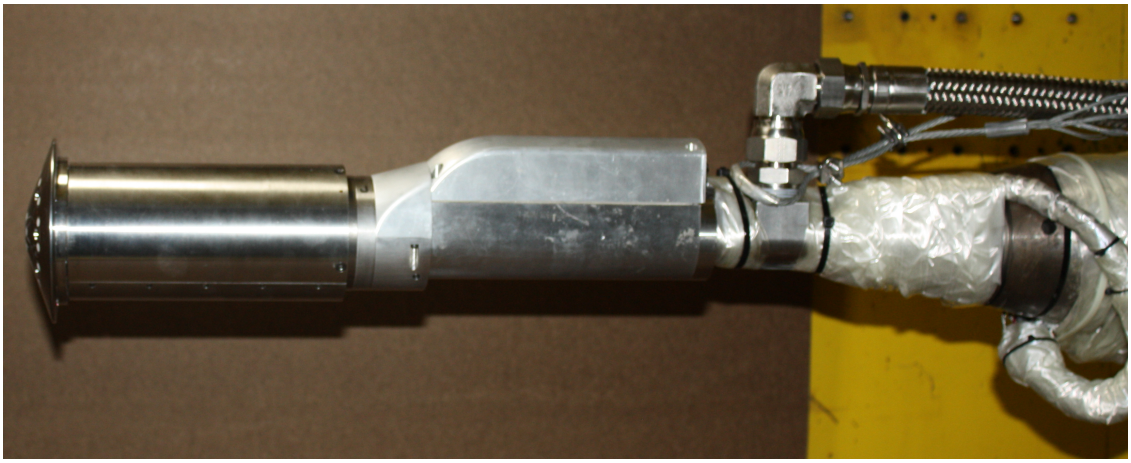

(c) Wind tunnel model

Fig. 4 HIAD/LUPWT overset grid system for OVERFLOW SRP simulations

The inflow BC to the test section for use in the DSS vehicle CFD work was obtained from simulations of the "full" wind tunnel geometry with an empty test section, which were performed by several groups in the AETC effort, including calculations done with OVERFLOW [27]. Initial simulations of the LUPWT geometry demonstrated that the test section flow cannot be idealized by neglecting the inflow boundary layers and subtle nonuniformity of the true test section flow. The upwash angle of the flow due to the upstream asymmetric wind tunnel nozzle-block expansion was shown to be as great as one degree in magnitude, and there are also weak, wake-like features from hardware in the settling chamber that survive passage through the wind tunnel nozzle-block throat and influence the test section flow. In the full-empty-tunnel simulations, the truncated LUPWT circuit, shown in Fig. 4a, was extended to include the settling chamber upstream of the test section, with internal geometry features of approximately one inch or larger modeled. Multiple instantaneous solutions at the inflow plane to the test section were extracted and averaged to produce a steady CFD approximation of the true flow into the test section, which was used as the inflow BC for the test section-only simulations conducted for this paper.

OVERFLOW's built-in AMR capability was heavily leveraged to provide sufficient refinement across all relevant length scales of the complex and chaotic DES SRP flowfield. Grid refinement was controlled regionally to improve the efficiency of the overall grid system, as OVERFLOW AMR is isotropic and yields a 2^{3N} growth rate for a given

mesh cell (where N is the AMR level). For this reason, AMR was limited aft of the vehicle heatshield, since the flow is supersonic and there should be minimal influence from downstream sting effects. Sufficient grid refinement was determined during the URANS flow initialization stage by setting successively finer levels of AMR, until the integrated loads on the vehicle converged to a constant value, as shown in Fig. 5a, where the vertical dashed lines represent the points at which successively finer levels of AMR were applied. Sufficient resolution to achieve an integrated heatshield drag force coefficient (C_D) converged to within $\Delta C_D = 0.003$ or 8 % was obtained for the HIAD with four levels of AMR in the SRP shock-plume interaction region, and two levels of adaption in the surrounding AMR Box region, resulting in the mesh refinement depicted in Fig. 5. It was also determined that this resolution could be maintained in all relevant areas of the flowfield with a maximum overall grid size limit of 300×10^6 points to improve simulation efficiency. Finally, due to the extremely dynamic nature of the SRP shock-plume interaction, it was also necessary to ensure that grid adaption was updated at a sufficiently-high enough frequency to capture any spatial variations in the flowfield over time, which was achieved for this flow application with an adaption cycle every 50 time steps.

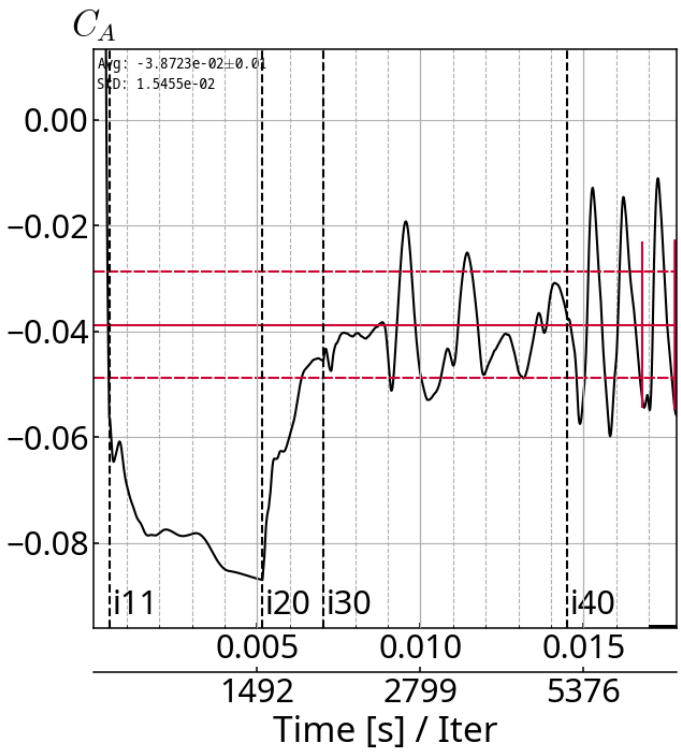

(a) Convergence of URANS AMR mesh

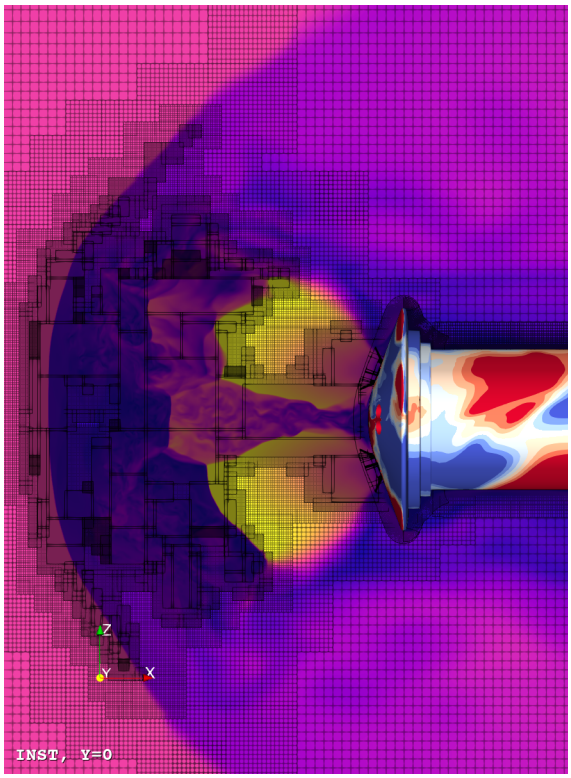

(b) Fully-refined DES AMR $y = 0$ mesh

Fig. 5 Grid convergence of OVERFLOW DES HIAD simulations

III. Results and Comparisons

This section reports the post-test OVERFLOW DES CFD results for the HIAD 1F nozzle configuration for the WTT test section condition $M = 3.5, C_T = 1.89$ at two angles $\alpha = \{0°, -10°\}$. Specific SRP flow phenomena are qualitatively and quantitatively compared between simulation and experiment.

A. Mean Supersonic Retropropulsion Flowfield

The time-averaged SRP flow properties are analyzed here to establish general characteristics and trends associated with each selected condition and to assess quantitative accuracy of CFD flowfield predictions.

1. Mean Schlieren Comparisons

Schlieren imaging is the only off-body data recorded in this experiment and allows for the visualization of the bow shock and plume structure during the test. Mean schlieren images are compared between the WTT and CFD for both conditions in Fig. 6. Averaged computed flowfield Mach number contours and heatshield surface pressure coefficient (C_P) distribution are also compared and are discussed in the following Sections.

For the $\alpha = 0°$ condition, the WTT mean bow shock shape (Fig. 6a) is smoothly convex and generally symmetric about the vehicle with a centerline standoff distance of $\approx 2.25D$, where D is the heatshield diameter. The analogous CFD prediction in Fig. 6c is averaged over a longer interval and indicates that are two primary modes for the bow shock shape. The further extent is more similar to the mode captured in the WTT in terms of both bow shock shape and standoff distance ($\approx 2D$). For both data sources, the oblique shocks of the engine plumes coalesce across the crossflow direction into a distinct "V" shape.

The $\alpha = -10°$ mean schlieren, depicted for the WTT and CFD in Figs. 6b and 6d, respectively, show an asymmetric, convex bow shock shape. Both sources have comparable standoff distances on the order of $\approx 1.25D$ (some uncertainty is associated with the WTT value due to image interference from the structural bars on the wind tunnel windows).

2. Mean Flowfield Predictions

Figures 6e and 6f compare the mean schlieren images discussed in Section III.A.1 to mean contours of the CFD-predicted flowfield Mach number for the zero and non-zero α conditions, respectively. The images also depict streamlines and surface C_P of the wind tunnel model and truncated sting. The multiple bow shock modes for the $\alpha = 0°$ case are apparent as different continuous regions in the averaged contours, where the shorter extent is defined by the purely-subsonic regions and the further extent is slightly greater than $M = 1$. The structure of the supersonic rocket plumes is readily observed, with strong oblique shocks defining the cores of the plumes emanating from the upper and lower nozzle pairs, which terminate in a normal shock. For this notionally-symmetric condition, it can be assumed that the plumes of the lateral engine pairs are similar in average shape. In the center of the flow, there is a barrel shock and Mach disk structure joining the four plume cores that corresponds to the "V" seen in the schlieren images.

The $\alpha = -10°$ mean M contours depict a local concavity in the bow shock, which indicates the average vertical position of the point of inflection in the oscillation interaction between the upper and lower plumes. The volume of the averaged plume cores is significantly reduced from the $\alpha = 0°$ case, which is likely due to the more significant unsteadiness over the averaging window.

3. Mean Heatshield Pressure Distribution

Figures 6g and 6h show the predicted mean heatshield pressure coefficient (C_P) distribution corresponding to the flowfield images discussed in the previous Sections. In the $\alpha = 0°$ case, the average pressure distribution is roughly symmetric, with a high pressure region in the center of the heatshield between the engine pairs and relatively low pressure across the outboard regions of the heatshield, excepting the shoulder regions at quadrants radially equidistant from engine pairs. The low net pressure on the heatshield indicates that the majority of vehicle deceleration performance in this flight condition would be due to thrust rather than blunt body drag. (It should be noted that the base pressure of this blunt body is expected to be relatively constant, so analysis of the heatshield-only pressure distribution is considered a good analog for high-level assessment of vehicle aerodynamics). The high pressure edges indicate areas that are momentarily outside of the influence of the plumes as they oscillate in location over the averaging window, which is more directly visualized in Section III.B.3 in Figs. 9j-9l. The upper right quadrant of the CFD mean prediction is notably different than the other three quadrants, which indicates that the average may not be fully converged over the averaging window that was selected for the mean flow calculation, and that this simulation would be improved by additional convergence.

The surface C_P distribution for the $\alpha = -10°$ case is asymmetric, as expected, with a lower-pressure windward region, where the bow shock is displaced further upstream and higher pressure on the windward side and in the stagnation region inboard of the nozzles. The computational average for this condition would also benefit from additional convergence, as indicated by the slight lateral asymmetry of the pressure distribution.

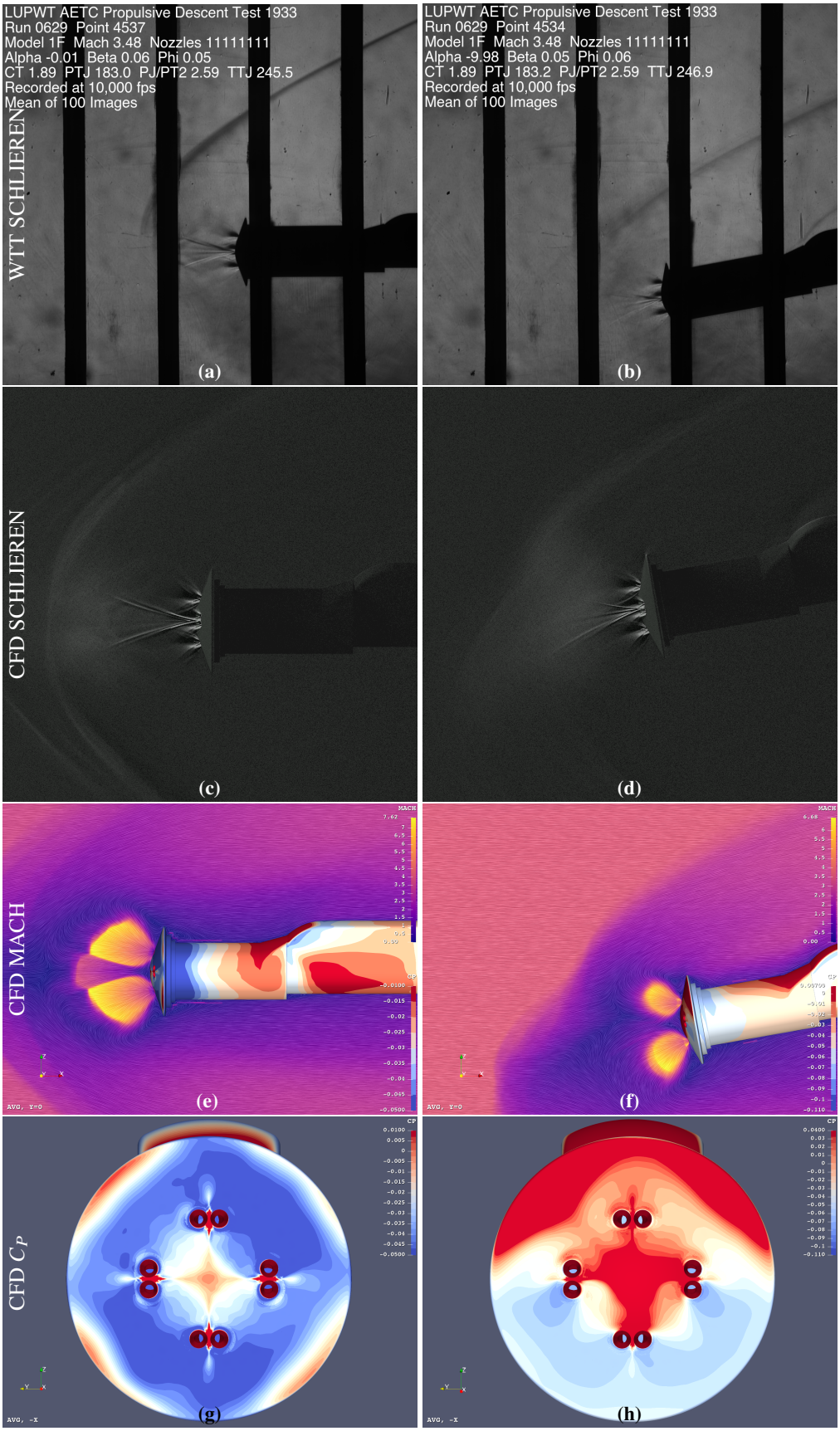

Fig. 6 Comparison of OVERFLOW DES and experimental mean flowfield ($M = 3.5, C_T = 1.89, \alpha = \{0°, -10°\}$)

4. Static Pressure Tap Comparisons

The quantitative accuracy of CFD flowfield predictions can also be assessed by comparing the static pressure at discrete locations on the vehicle surface to time-averaged tap measurements in the experiment. The locations of the WTT static pressure taps on the heatshield are indicated in Fig. 7a (additional taps are located on the backshell and sting in the base pressure region). CFD C_P results are depicted with variance bars indicating $\pm 1SD$ standard deviation over the time-averaging window. WTT static taps are not accurate for high-frequency measurements, so averaging statistics are not reported for these data. SRP flowfield unsteadiness will be discussed in more detail in Section III.B.

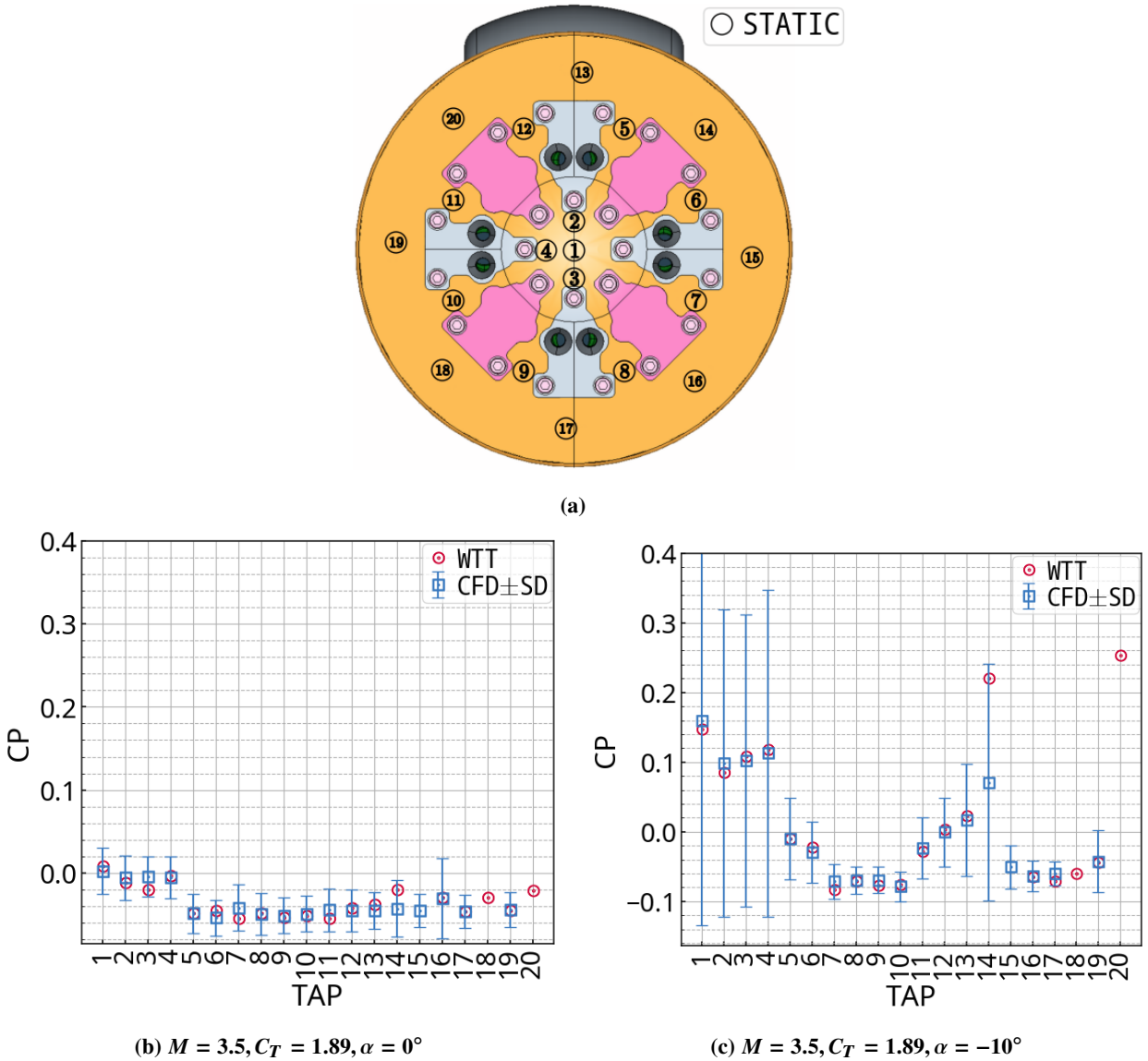

(a)

(b) $M = 3.5, C_T = 1.89, \alpha = 0°$

(c) $M = 3.5, C_T = 1.89, \alpha = -10°$

Fig. 7 Comparison of OVERFLOW DES and experimental mean static pressure tap data with time standard deviation variation bars

Considering first the $\alpha = 0°$ case in Fig. 7b, Taps 1-4 correspond to the stagnation region inboard of the nozzles and record relatively small pressure signals. Due to these low signals, there is a significant percent difference in values between CFD and WTT of $|\Delta C_P| \approx 70\,\%$. The next family of sensors are Taps 5-12, which are equally spaced angularly at a radius just outboard of the nozzles. These sensors all show a more negative C_P level than the stagnation sensors and a more comparable percent difference of $|\Delta C_P| \approx 11\,\%$. The final family of heatshield static pressure sensors are

Taps 13-20, which are located nearer the heatshield shoulder. For this condition, the WTT data showed more variation than predicted by CFD between sensors radially-aligned with nozzle pairs and sensors located halfway between. At locations aligned with the nozzle pairs, the CFD was only $|\Delta C_P| \approx 3.4\,\%$ from the WTT data, while $|\Delta C_P| \approx 100\,\%$ for the sensors in between nozzles with significancy lower pressure levels.

For the $\alpha = -10^\circ$ case, the stagnation pressure is significantly greater, and the percent differences for Taps 1-4 are correspondingly lower ($|\Delta C_P| \approx 9\,\%$). C_P accuracy at the nozzle radius is similar to the $\alpha = 0^\circ$ case with $|\Delta C_P| \approx 12\,\%$ (excluding Tap 12, where the measured $C_P \sim 0$). Heatshield shoulder tap accuracy also followed similar trends to the previous condition, with nozzle-alined taps $|\Delta C_P| \approx 11\,\%$ and adjacent taps $|\Delta C_P| \approx 100\,\%$.

B. Unsteady Supersonic Retropropulsion Flowfield

Notable flow unsteadiness was observed at many test conditions and was characterized by dynamic bow shock shape modulations that resulted in both high-frequency fluctuations and long-period modulations of the surface pressure distribution.

1. Instantaneous Schlieren Comparisons

Instantaneous schlieren images provide insight into the variations of the flowfield over time and provide elaboration for some of the inferences made in the section on mean schlieren results. Results for the $\alpha = 0^\circ$ case are shown in Fig. 8. The first column (Fig. 8a) corresponds to an instant that is generally similar to the mean nature of the flow shown earlier in Fig. 6a. The bow shock shape is generally smooth and convex, but is subject to more local variation than the average. There is also significantly more detail to the SRP shock-plume interaction region. The second column (Fig. 8b) depicts an unsteady fluctuation of the bow shock just below the centerline, which is qualitatively replicated by the DES CFD in Fig.8e. The third column (Fig. 8c) shows a minor variation, where the plumes locally exceed the main curve of the bow shock just above the centerline. In real-time video visualization, this is the beginning of a pulsation of the bow shock momentarily away from the vehicle surface that occurs as a rippling, downstream propagation of that initial extension of the bow shock standoff distance. This periodic pulsation of the bow shock also occurs in the CFD in Fig. 8f.

Figure 9 depicts similar results for the $\alpha = -10^\circ$ condition. Here, the bow shock point of inflection described in Section III.A.2 is more readily apparent in Figs. 9a and 9d. The downstream propagation of these variations in the bow shock can be observed in Figs. 9b and 9e, where the point of inflection has split into two separate "lobes", with a distinct Mach disk and barrel shock at the center of both the WTT and CFD images. Lastly, as discussed in Section III.A.1, it is apparent by comparing Figs. 9a and 9c that there is significant fluctuation in the standoff distance of the leeward portion of the bow shock. The DES CFD qualitatively replicates these bulk, time-varying changes in standoff distance within 10 %, but exact replication of this complex and dynamic phenomena with CFD is challenging. Local, qualitative differences are apparent in the instantaneous comparisons between WTT and CFD, as with the upper shock lobe heights in Figs. 9b and 9e and the almost-normal shape of the CFD bow shock in Fig. 9f, which differs from the more rounded WTT bow shock in Fig. 9c.

2. Unsteady Flowfield Predictions

As with the mean flow in Section III.A.2, M-contour plots of the $y = 0$ instantaneous flow are compared to the schlieren images in Figs. 8 and 9. Figures 8g-8i for the $\alpha = 0^\circ$ case show subtle variations in the topology of the plume termination shocks, indicating the highly unsteady and non-linear nature of the SRP interaction. Figures 9g-9i for the $\alpha = -10^\circ$ condition depict the significant variation in the expansion of the leeward plume, which doubles in core size during the periodic fluctuation.

3. Unsteady Heatshield Pressure Distribution

The unsteady effect of flow fluctuations on heatshield pressure distribution is also compared in Figs. 8 and 9. The slight, local fluctuations in the bow shock shape of the $\alpha = 0^\circ$ case result in sweeping variations of the heatshield C_P from the baseline near-zero value (Fig. 8j). These variations are indeterminate due to the symmetric nature of the flow condition. The $\alpha = -10^\circ$ case (Figs. 9j-9l) also experiences surface pressure fluctuations, but primarily on the windward side of the heatshield, while the leewards side remains comparatively constant within the extended bow shock.

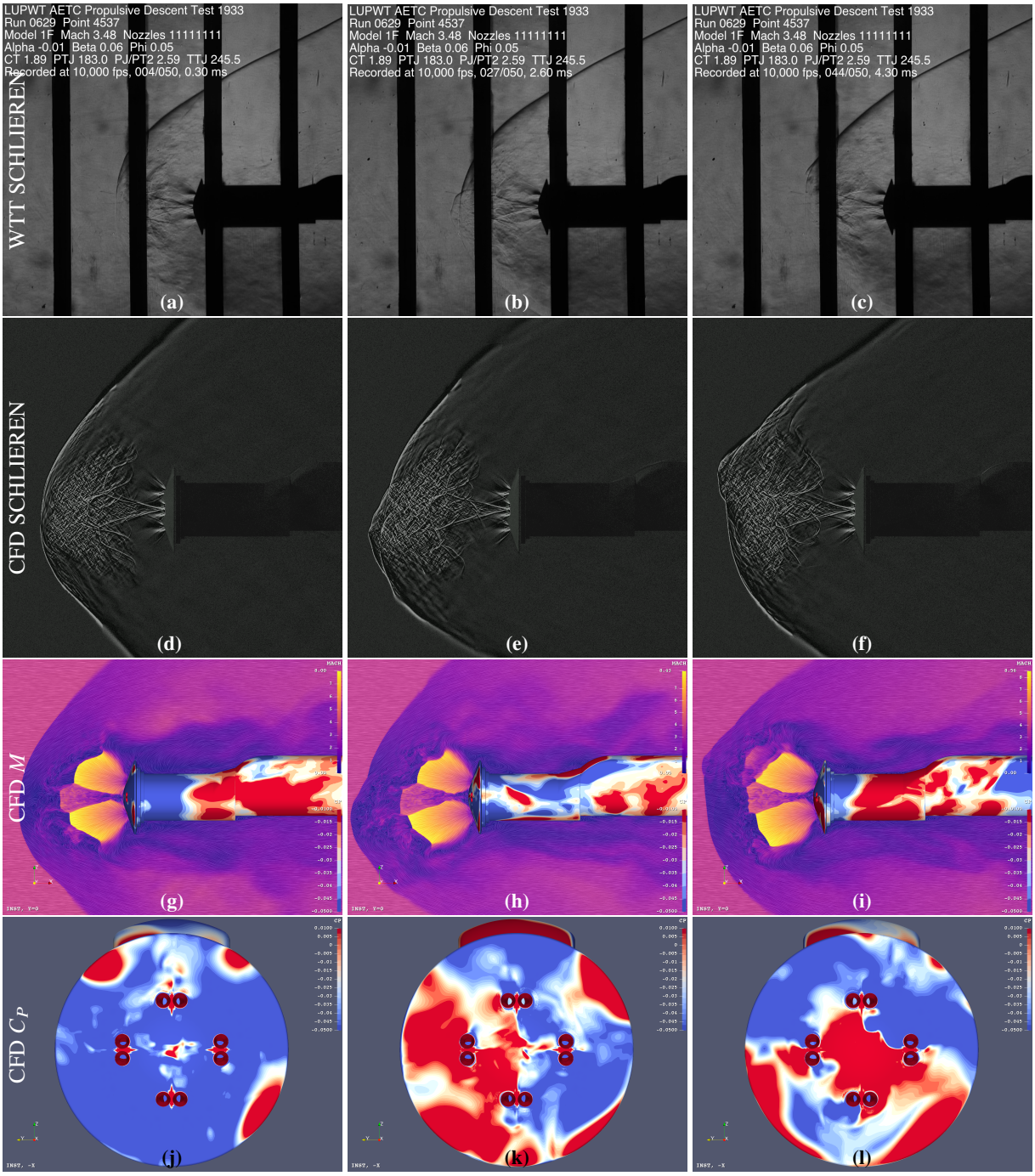

Fig. 8 Comparison of OVERFLOW DES and experimental unsteady flowfield ($M = 3.5, C_T = 1.89, \alpha = 0°$)

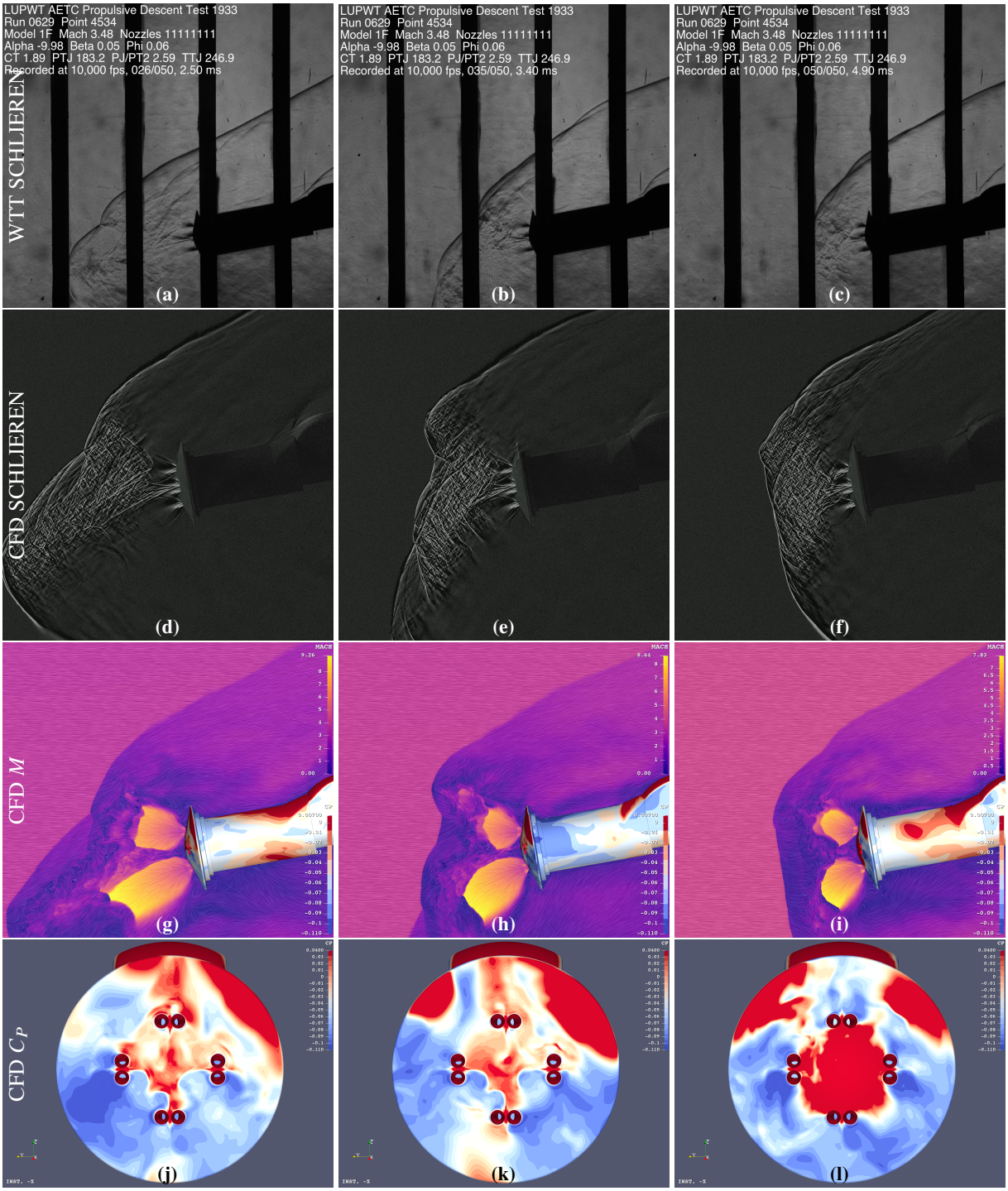

Fig. 9 Comparison of OVERFLOW DES and experimental unsteady flowfield ($M = 3.5, C_T = 1.89, \alpha = -10°$)

4. Unsteady Pressure Tap Comparisons

Flow unsteadiness during the experiment can be quantitatively analyzed using discrete measurements of C_P recorded with high-frequency kulite® pressure sensors. Locations of the dynamic kulites® on the heatshield are indicated in Fig. 10a. As with the static taps, there are three distinct spatial regions on the heatshield where kulites® are located:

stagnation (kulite® 1), nozzle-radius (kulite® 2), and heatshield edge (kulites® 11-14). However, the nozzle-radius kulite® 2 was non-functional in the test, so comparison data is unavailable at that location. Similar to the static taps, additional kulites® are located on the backshell and sting in the base pressure region. By design, the accuracy of the dynamic kulite® measurements' mean value is poor relative to that of the static taps, so comparisons between WTT and CFD results are made in Figs. 10b and 10c in terms of the standard deviation over the time-averaging window, which is a quantitative measurement of the flow unsteadiness. Plot limits are set to twice the maximum C_P value recorded by the static taps to provide perspective of the relative significance of each unsteadiness magnitude.

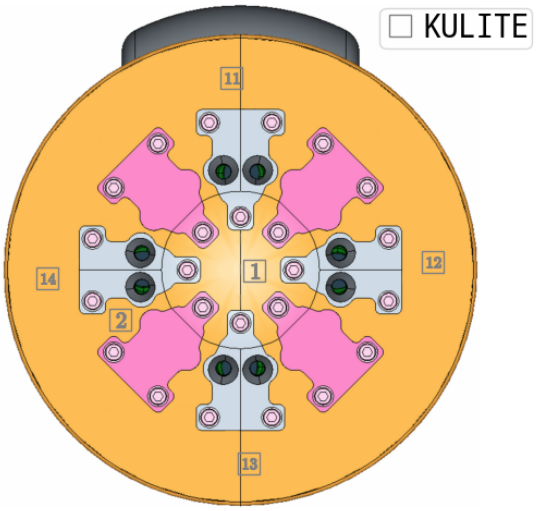

(a)

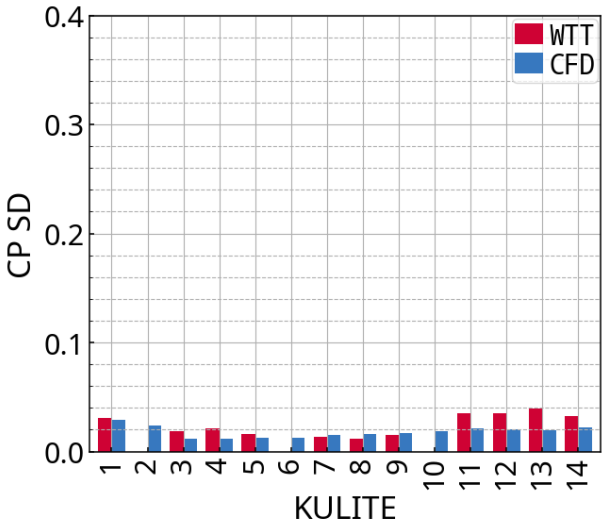

(b) $M = 3.5, C_T = 1.89, \alpha = 0°$

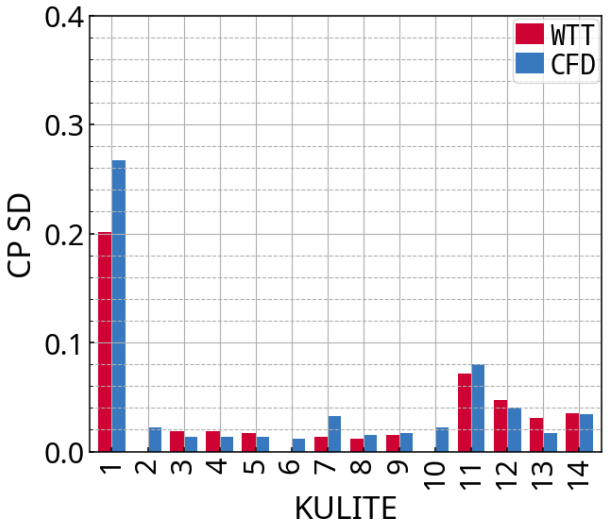

(c) $M = 3.5, C_T = 1.89, \alpha = -10°$

Fig. 10 Comparison of OVERFLOW DES and experimental unsteady pressure tap data

Results for the $\alpha = 0°$ condition are shown in Fig. 10b. For this symmetric case, where the mean C_P of the heatshield is relatively constant and minimal, the magnitude of unsteadiness recorded by kulite® 1 in the stagnation region is similar to the other regions. CFD also predicts a similar level of unsteadiness in the region, with $|\Delta SD_{C_P}| \approx 6\,\%$. Unsteadiness at the heatshield shoulder (kulites® 11-14) was generally uniform for this symmetric case for both the experimental and computational results, however, the unsteadiness at the shoulder in the experiment was significantly greater ($|\Delta SD_{C_P}| \approx 40\,\%$).

The $\alpha = -10^\circ$ condition (Fig. 10c) was strongly unsteady in the stagnation region for both the WTT and CFD, and the relative difference was proportionally high ($|\Delta SD_{C_P}| \approx 30\,\%$), though with the simulation showing greater unsteadiness in this instance. Both the WTT and CFD showed varying unsteadiness magnitude around the heatshield shoulder (kulites® 11-14), with unsteadiness increasing from leeward to windward, while magnitudes were within $|\Delta SD_{C_P}| \approx 18\,\%$.

Overall, the DES CFD predictions of unsteadiness showed similarity to that of the experiment, especially considering the highly dynamic and complex nature of this flow application. Additional convergence of the unsteady solution would potentially yield improved comparison.

IV. Conclusion

This paper presented comparisons of experimental data and Overflow CFD results for supersonic retropropulsion (SRP) conditions over a blunt Mars EDL vehicle. Two test conditions were selected for detailed analysis with Detached Eddy Simulation (DES) turbulence modeling at $M = 3.5, C_T = 1.89, \alpha = \{0^\circ, -10^\circ\}$. Both SRP conditions demonstrated significant flow unsteadiness in both the experimental and simulated results. Comparisons of WTT and CFD averaged and instantaneous schlieren imaging demonstrated comparability in the general shape of the bow shock as well as specific, time-varying fluctuations of the shock-plume interaction. Comparisons of discrete, time-averaged, surface pressure measurements showed good CFD accuracy within approximately 10 % of experimental measurements across the majority of the heatshield, but more significant difference was observed at some of the locations on the heatshield shoulder where the flow displayed maximal unsteadiness. Unsteadiness of the CFD quantified by C_P standard deviation (SD) showed a more notable difference of 20-40 % from experimental measurements due to the extremely dynamic nature of this flow. Overall, these comparisons demonstrate that Overflow DES CFD can provide reasonable predictions of the general mean and unsteady properties of highly dynamic and multi-modal flows like this SRP application at specific conditions, though exact replication of all specific unsteady behaviors observed in the test still proves challenging.

In future comparisons, CFD accuracy could be further improved with additional temporal convergence to minimize asymmetry due to flow unsteadiness over the time averaging window. Richer experimental data sets would also improve the confidence in CFD quantitative validation and uncertainty quantification. Specifically, PSP data would allow for a more continuous comparison across the entire vehicle surface, and balance data would allow the assessment of CFD nozzle thrust prediction accuracy.

Acknowledgments

This work is supported by the joint effort between NASA's Aerosciences Evaluation and Test Capabilities (AETC) program office under the Aeronautics Research Mission Directorate (ARMD) and the Game Changing Development (GCD) program's Descent System Study (DSS) under the Space Technology Mission Directorate (STMD). CFD simulations were run on NASA Advanced Supercomputing Division resources and were funded by the GCD program's DSS. The authors thank the AETC and DSS teams for their advice and collaboration and J. Garcia and K. Matsuno for their review of this research.

References

[1] Sell, S. W., Davis, J. L., Miguel San Martin, A., and Serricchio, F., "Powered Flight Design and Performance Summary for the Mars Science Laboratory Mission," *Journal of Spacecraft and Rockets*, Vol. 51, No. 4, 2014, pp. 1197–1207. https://doi.org/10.2514/1.A32682.

[2] Cianciolo, A., Korzun, A., Samareh, J., Sostaric, R., Calderon, D., and Garcia, J., "Human Mars Entry, Descent, and Landing Architecture Study: Phase 3 Summary," 2020.

[3] Cerimele, C. J., Robertson, E. A., Sostaric, S. R., Campbell, C. H., Robinson, P., Matz, D. A., Stachowiak, S. J., Garcia, J. A., Bowles, J. V., Kinney, D. J., and Theisinger, J. E., "A rigid mid-lift-to-drag ratio approach to human Mars entry, descent, and landing," *AIAA Guidance, Navigation, and Control Conference*, 2017, p. 1898.

[4] Cianciolo, A. D., Dillman, R., Brune, A., Lugo, R., Polsgrove, T., Percy, T. K., Sutherlin, S., and Cassell, A., "Human Mars Entry, Descent and Landing Architecture Study: Deployable Decelerators," *AIAA SPACE*, 2018.

[5] Edquist, K. T., Falman, B. E., Burns, D. E., Watkins, A. N., Pham, H. T., and Houlden, H. P., "Testing of Two Mars Powered Descent Vehicle Concepts in the Langley Unitary Plan Wind Tunnel," *AIAA Aviation Forum*, 2024.

[6] Ross, J. C., Rhode, M. N., Falman, B., Edquist, K., Schoenenberger, M., Brauckmann, G. J., Kleb, W. L., West, T., Alter, S. J., and Witte, D., "Evaluation of CFD as a Surrogate for Wind-Tunnel Testing for Mach 2.4 to 4.6-Project Overview," *AIAA AVIATION 2021 FORUM*, 2021, p. 2961.

[7] Moran, P., "Computational Schlieren with Comparisons to Experiment," *International Symposium on Flow Visualization ISFV*, 2018.

[8] Edquist, K., Glass, C., Korzun, A., Wood, W., West, T., Alter, S., Canabal, F., Childs, R., Halstrom, L., and Matsuno, K., "Computational Analysis of Two Mars Powered Descent Vehicle Concepts Tested in the Langley Unitary Plan Wind Tunnel," *AIAA Aviation Forum*, 2024.

[9] Matsuno, K., Childs, R., Pulliam, T., Stremel, P., Garcia, J., and Moran, P., "Comparison of OVERFLOW Computational and Experimental Results of the CobraMRV Mars Entry Vehicle Concept during Supersonic Retropropulsion," *Submitted to AIAA Aviation 2024 Forum*, 2024.

[10] Halstrom, L. D., Pulliam, T. H., Childs, R. E., and Stremel, P. M., "OVERFLOW Analysis of Supersonic Retropropulsion Testing on a Blunt Mars Entry Vehicle Concept," *Submitted to AIAA Scitech 2022 Forum*, 2022.

[11] Buning, P. G., "NASA OVERFLOW CFD Code," https://overflow.larc.nasa.gov/, 2021. Accessed: 2021-05-20.

[12] Buning, P. G., Jespersen, D. C., Pulliam, T. H., Chan, W., Slotnick, J. P., Krist, S., and Renze, K. J., "Overflow user's manual," *NASA Langley Research Center, Hampton, VA*, 2002.

[13] Nichols, R., Tramel, R., and Buning, P., "Solver and turbulence model upgrades to OVERFLOW 2 for unsteady and high-speed applications," *24th AIAA Applied Aerodynamics Conference*, 2006, p. 2824.

[14] Nichols, R. H., and Buning, P. G., "User's Manual for OVERFLOW 2.1," *University of Alabama and NASA Langley Research Center*, 2008.

[15] Rogers, S., Roth, K., Nash, S., Baker, M., Slotnick, J., Whitlock, M., and Cao, H., "Advances in overset CFD processes applied to subsonic high-lift aircraft," *18th Applied Aerodynamics Conference*, 2000, p. 4216.

[16] Chan, W., "The overgrid interface for computational simulations on overset grids," *32nd AIAA Fluid Dynamics Conference and Exhibit*, 2002, p. 3188.

[17] Chan, W., "Developments in Strategies and Software Tools for Overset Structured Grid Generation and Connectivity," *20th AIAA Computational Fluid Dynamics Conference*, 2011, p. 3051.

[18] Meakin, R., "Object X-rays for cutting holes in composite overset structured grids," *15th AIAA Computational Fluid Dynamics Conference*, 2001, p. 2537.

[19] Chan, W. M., Kim, N., and Pandya, S. A., "Advances in domain connectivity for overset grids using the x-rays approach," 2012.

[20] Menter, F. R., "Two-equation eddy-viscosity turbulence models for engineering applications," *AIAA journal*, Vol. 32, No. 8, 1994, pp. 1598–1605.

[21] Childs, R., Garcia, J., Melton, J., Rogers, S., Shestopolov, A., and Vicker, D., "Overflow Simulation Guidelines for Orion Launch Abort Vehicle Aerodynamic Analyses," *29th AIAA Applied Aerodynamics Conference*, 2011, p. 3163.

[22] Childs, R. E., Garcia, J. A., Rogers, S. E., and Vicker, D. J., "Overflow Aerodynamic Simulation of the Orion Launch Abort Vehicle," *Joint Army Navy NASA Air Force*, 2013.

[23] Mani, M., Babcock, D., Winkler, C., and Spalart, P., "Predictions of a supersonic turbulent flow in a square duct," *51st AIAA Aerospace Sciences Meeting including the New Horizons Forum and Aerospace Exposition*, 2013, p. 860.

[24] Spalart, P. R., "Strategies for turbulence modelling and simulations," *International journal of heat and fluid flow*, Vol. 21, No. 3, 2000, pp. 252–263.

[25] Childs, R., and Matsuno, K., "Novel Turbulence Model Tailored for Rocket Motor Exhaust Jets," *Submitted to AIAA Aviation 2024 Forum*, 2024.

[26] Welford, BP., "Note on a Method for Calculating Corrected Sums of Squares and Products," *Technometrics : a journal of statistics for the physical, chemical, and engineering sciences*, Vol. 4, No. 3, 1962, pp. 419–420.

[27] Childs, R., Stremel, P., Hawke, V., Garcia, J., Kleb, W. L., Hunter, C., , Parikh, P., Patel, M., Alter, S. J., Rhode, M. N., and Salari, K., "Flow Characterization of the NASA Langley Unitary Plan Wind Tunnel, Test Section 2: Computational Results," *AIAA AVIATION 2021 FORUM*, 2021, p. 2963.